https://doi.org/10.2352/EI.2024.36.15.COIMG-143

Multimodal Deep Learning Approach for Dynamic Sampling with Automatic Feature Selection in Matrix-Assisted Laser Desorption/Ionization Mass Spectrometry Imaging

David Helminiak; Electrical and Computer Engineering, Marquette University; Milwaukee, Wisconsin, USA
Tobias Boskamp; Bruker Corporation; Bremen, Germany
Dong Hye Ye; Computer Science, Georgia State University; Georgia, USA

Abstract

Acquisitions of mass-per-charge (m/z) spectrometry data from tissue samples, at high spatial resolutions, using Mass Spectrometry Imaging (MSI), require hours to days of time. The Deep Learning Approach for Dynamic Sampling (DLADS) and Supervised Learning Approach for Dynamic Sampling with Least-Squares (SLADS-LS) algorithms follow compressed sensing principles to minimize the number of physical measurements performed, generating low-error reconstructions from spatially sparse data. Measurement locations are actively determined during scanning, according to which are estimated, by a machine learning model, to provide the most relevant information to an intended reconstruction process. Preliminary results for DLADS and SLADS-LS simulations with Matrix-Assisted Laser Desorption/Ionization (MALDI) MSI match prior 70% throughput improvements, achieved in nanoscale Desorption Electro-Spray Ionization (nano-DESI) MSI. A new multimodal DLADS variant incorporates optical imaging for a 5% improvement to final reconstruction quality, with DLADS holding a 4% advantage over SLADS-LS regression performance. Further, a Forward Feature Selection (FFS) algorithm replaces expert-based determination of m/z channels targeted during scans, with negligible impact to location selection and reconstruction quality.

Introduction

Matrix-Assisted Laser Desorption/Ionization (MALDI) Mass Spectrometry Imaging (MSI) provides label-free measurements of signal intensities, across a range of mass-per-charge (*m/z*) channels, at high spatial resolutions. MALDI MSI has become an important tool in biological and chemical analyses for life science research and clinical pathology [1]. While at microscopic resolutions, MSI can require hours to days for complete acquisitions, combining known data, from sparse spatial sampling, with reconstructed values, derived thereof, can massively improve throughput. ~60-95% reductions in the number of required measurements, for multiple imaging technologies, have already been achieved with variants of a Supervised Learning Approach for Dynamic Sampling (SLADS) [3] [4], using least-squares regression (SLADS-LS) [5] [6] [7], a multilayer perceptron network (SLADS-Net) [8], and unsupervised hierarchical Gaussian mixture models (U-SLADS) [15]. Leveraging multiple channels of *m/z* data, re-implementations of SLADS-LS, SLADS-Net, and a novel Deep Learning Approach for Dynamic Sampling (DLADS) [9] [10], using a Convolutional Neural Network (CNN), improved throughput for nanoscale Electro-Spray Ionization (nano-DESI) MSI by ~70% in simulations [11] and ~44% in actual integration [12]. Both SLADS and DLADS dynamically select sparse sets of measurement locations during active acquisitions, through trained machine learning models, to maximize the quality of derived reconstructions.

Advancement on Prior Work

Novel advancements made in this study include: 1) the simulated application of DLADS and SLADS-LS to MALDI MSI, 2) the creation of a multimodal DLADS variant to incorporate optical imaging in measurement location selection, and 3) a procedural method for determining a limited set of representative *m/z* during training, later used in the location selection process.

1) Nano-DESI MSI platforms commonly acquire spectra across 2D samples in a static raster pattern. Integration with DLADS was encumbered by a proprietary control mechanism, restricting measurement selections to contiguous segments along a singular axis, reducing realizable throughput gains by ~30%. MALDI MSI platforms are less restrictive on measurement location selection, such that simulations are likely more indicative of realizable gains.

2) The MALDI MSI equipment utilized for this work automatically performs optical imaging and semantic segmentation on examined specimens. Thereby, locations within the equipment Field of View (FoV), without physical material, are not scanned from the outset. Multimodal DLADS similarly restricts the measurement area, according to the available mask, and utilizes the optical image as an input feature for optimal scan location selection.

3) For each spatial measurement location, MSI acquires a data quantity prohibitive to analyses needed for dynamic sampling, where computational resources are a critical bottleneck. DLADS for MSI therefore only processes a selection of *m/z* channels during actual scans. These target *m/z* must be chosen in advance of model training or experimental implementation and ideally be highly representative of experimental objectives. Prior works relied on manual selection by a domain expert, injecting potential inconsistencies, human bias, and becoming problematic for data at scale. While dimension reduction strategies can be successful [13], they require intensity thresholding to reduce the problem complexity, thereby removing any low-intensity patterns from consideration. A Forward Feature Selection (FFS) process, inspired by Sequential Feature Selector (SFS) algorithms [17], mitigates these issues, choosing relevant and diverse representative target *m/z*, demonstrating equivalent sampling performance to expert choices.

Methods

Dynamic Sparse Sampling

The SLADS-LS and DLADS algorithms follow multichannel implementations developed for nano-DESI MSI [11]. For each MSI sample, there exists a set of L representative target *m/z*: Z. Every channel $z \in Z$ denotes a mass range (1), with a peak width: Δ ppm (parts-per-million). Integrating measured intensities in these ranges, across the equipment's FoV, forms 2D ground-truth *m/z* images: X_Z.

$$[z \cdot (1 - \Delta \cdot 10^{-6}), z \cdot (1 + \Delta \cdot 10^{-6})] \quad (1)$$

During acquisition there exist unmeasured and measured location sets: T and S, where values for $t \in T$ are estimated with Inverse Distance Weighted (IDW) [20] mean interpolation, forming a channel reconstruction set: $\hat{X}_Z$. An unmeasured location to be scanned next: $\bar{t}$, may be selected by (2), which seeks to minimize the absolute error between X_z and $\hat{X}_z$, averaged across all $z \in Z$.

$$\bar{t} = \underset{t \in T}{argmin}\{\frac{\sum_{z \in Z}|X_z^{S \cup t} - \hat{X}_z^{S \cup t}|}{L}\} \quad (2)$$

A set of Reduction in Distortion (RD) maps: R_Z (3) quantifies the spatial distribution of this ideal information gain. RD for measured locations: $R_Z^S = 0$. Using the foreground mask generated by MALDI equipment, multimodal DLADS sets the RD at each background site ($b \in B$): $R_Z^B = 0$ (dilated with a 3-by-3 kernel for training). For each remaining $t \in T$: R_z^t equals the sum improvement in $\hat{X}_z$ resultant of measuring that position ($S \cup t$). The RD map used to determine $\bar{t}$, averages across $z \in Z$: $R = \sum_{z \in Z}(R_z)\,/L$.

$$R_Z = \begin{cases} \sum\left(\left|X_z - \hat{X}_z^S\right| - \left|X_z - \hat{X}_z^{S \cup t}\right|\right) : \forall t \in T \\ 0 : \forall s \in S \\ 0 : \forall b \in B \end{cases} : \forall z \in Z \quad (3)$$

The computational expense of reconstruction necessitates approximating the RD (4), as the sum of the absolute difference between the ground-truth X_z and current reconstruction $\hat{X}_z$ multiplied by a 2D Gaussian $G(\cdot)$, centrally applied at t, having strength σ^t (5), and radius: r^t (6). σ^t equals the nearest measured neighbor distance divided by a regularization parameter: c.

$$R_z^T \approx \left\{\sum\left(\left|X_z - \hat{X}_z\right| \cdot G(t, \sigma^t, r^t)\right) : \forall t \in T\right\} \quad (4)$$

$$\sigma^t = \frac{\min_{s \in S}\|s - t\|}{c} \quad (5)$$

$$r^t = 2 \cdot \left\lceil \frac{(3\sigma^t - 1)}{2} \right\rceil \quad (6)$$

For each training sample and potential $c \in \{1, 2, 4, 8, \ldots, 256\}$, following an initial 1% random spatial sampling, measurements are made up to 30% FoV, using R, generated with said c value, as the selection mechanism. Integrating the Peak Signal to Noise Ratio (PSNR) [16] of $\hat{X}_Z$ at 1% intervals forms an Area Under Curve (AUC) score, maximized by the optimal c tested.

X_Z and R_Z are not known during actual sampling, so machine learning models are used to compute a set of per-*m/z* Estimated RD (ERD) maps: $\hat{R}_Z$. After an initial 1% FoV random measurement for initialization, the next sampling location: $\bar{t} = max_{t \in T}(\hat{R}^t)$, where $\hat{R} = \sum_{z \in Z}(\hat{R}_z)\,/L$. Constraints that $\hat{R}_Z^S = 0$, and with multimodal DLADS: $\hat{R}_Z^B = 0$, are enforced at scan time. Sampling continues until $\sum\hat{R} = 0$, or a specified % FoV has been measured.

Random spatial sampling of target *m/z* images, extracted from the training samples (1% to 30% FoV at 1% intervals), with matched per-*m/z* approximated RD maps, generated using the optimized c value, forms a training database. SLADS-LS uses a least-squares regression model (7) to optimize parameters: $\hat{\theta}$ from hand-crafted, statistical features: V_z^T, extracted from $\hat{X}_z$, such that $\hat{R}_z^T = V_z^T \cdot \hat{\theta}$.

$$\hat{\theta} = \underset{\theta \in \mathbb{R}}{argmin}\|R^T - V^T \cdot \theta\|^2 \quad (7)$$

DLADS uses a Convolutional Neural Network (CNN) U-Net [19] architecture, with trained weights: w, and per-*m/z* input set: I_z, to perform an image-to-image translation: H, where $\hat{R}_z = H^w(I_z)$. I_z consists of the measured values: X_z^S, their positions: 1^S, reconstruction values for unmeasured locations: $\hat{X}_z^T$, and with multimodal DLADS, the complete optical image. The network trains to minimize a Mean Absolute Error (MAE) loss (8) between $\hat{R}_z$ and R_z, using a Nadam optimizer and a 10^{-5} learning rate.

$$Loss_{MAE} = |R_z - H^w(I_z)| \quad (8)$$

Target m/z Channel Selection

Across a training set of N fully acquired MSI samples (where $X_Z[n]$ denotes the *m/z* images for a sample index: $n \in \{1, \ldots, N\}$), there exists a set of spectrally non-overlapping *m/z*: $\bar{Z}$, with global lower and upper *m/z* limits: $[\bar{Z}_{low}, \bar{Z}_{high}]$, and peak width: Δ. For elucidation: $\bar{Z}^0 \mapsto [\bar{Z}^0_{low} = \bar{Z}_{low}, \bar{Z}^0_{high} = \bar{Z}^0_{low} \cdot (1 + \Delta \cdot 10^{-6})]$, where in the next range: $\bar{Z}^1_{low} = \bar{Z}^0_{high}$. Given a $\Delta = 20$ ppm, $\bar{Z}_{low} = 600$, and $\bar{Z}_{high} = 3200$ there exist ~42k *m/z* ranges. This quantity of data effectively prevents direct application of dynamic sampling models in MSI technologies. However, not all acquired *m/z* contain information critical to experimental objectives and many *m/z* exhibit similar spatial response patterns. Therefore, to maximize computational efficiency, sample spectra may be reduced to a sparse set of L target *m/z*: $Z \subset \bar{Z}$, representative of the structurally diverse information expected to be encountered during acquisition. Ideally, target *m/z* images should be orthogonal to one another and together represent global sample spectra semantics.

function $FFS(L, \bar{Z}, N, X_{\bar{Z}}[\{1, \ldots, N\}]) \mapsto Z$:

#Create an empty list to store chosen *m/z values*
$Z = [\,]$

#Create a list of 0 arrays, as per-sample comparison images
$A = [0^{size(X_1[n])} : \forall n \in \{1, \ldots, N\}]$

#Create a zero array to hold cumulative scores for each *m/z*
$F = 0^{size(\bar{Z})}$

#Loop until the desired number of *m/z* have been selected
while $size(Z) \neq L$ *do*:

#For each *m/z* and for each sample index
for $z \in \bar{Z}$: *for* $n \in \{1, \ldots, N\}$:

#Add the sum SSIM between comparison and *m/z* images
$F_z \mathrel{+}= SSIM(A[n], X_z[n])$

#Find the *m/z* with the lowest cumulative score
$z = \bar{Z}[argmin(F)]$

#Add the selected *m/z* to the final list of representative *m/z*
$Z.append(z)$

#Prevent potential future reselection of the selected *m/z*
$F_z = \infty$

#Set the next comparison images as those of the chosen *m/z*
$A = X_z$

Figure 1. *FFS pseudocode to find a set of L m/z: Z, representative of m/z set: $\bar{Z}$, shared for N fully acquired MSI samples, with visualizations: $X_{\bar{Z}}[\{1, \ldots, N\}]$.*

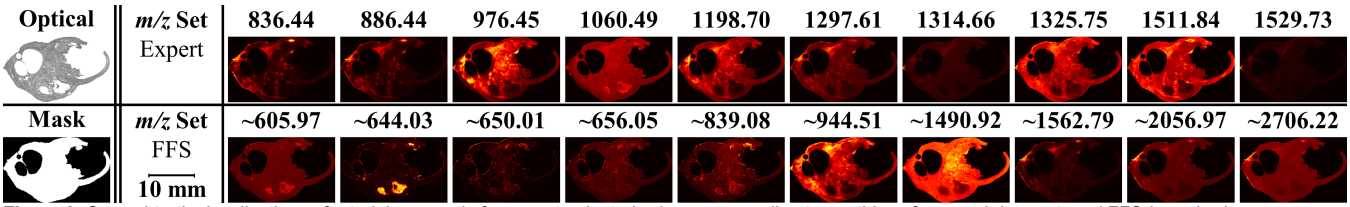

***Figure 2**. Ground-truth visualizations of a training sample for expert-selected m/z, corresponding to peptides of research interest, and FFS-based m/z, progressively determined though a computationally efficient SSIM-based FFS algorithm that seeks to maximize spectral representation and structural distinction.*

A Forward Feature Selection (FFS) algorithm (Fig. 1) was designed to objectively select L *m/z*: Z, from $\bar{Z}$, given N samples with images: $X_{\bar{Z}}[\{1, \dots, N\}]$, using the Structural Similarity Index Measure (SSIM) [14]. SSIM being selected as a common perceptual and structural metric. Summarily, the FFS iteratively adds *m/z*, not yet selected: $\{z \in \bar{Z}\} \cup \{z \notin Z\}$, whose visualizations across all samples, are least similar to current $z \in Z$. The process initializes variables: Z, being an empty set; A: a list of 0 arrays for initial comparison images (dimensions matched per-sample); and F: a list of cumulative scores for each $z \in \bar{Z}$. Looping until $size(Z) = L$, for each $z \in \bar{Z}$ and sample index $n \in \{1, \dots, N\}$, an SSIM score, between a current sample comparison array: $A[n]$, and considered *m/z* image: $X_z[n]$, gets added to F_z. The *m/z* with lowest cumulative score: $\bar{Z}[argmin(F)]$, becomes added to Z, its score set to infinite to prevent reselection, and replaces A with its corresponding *m/z* images. Overall, this method evaluates spectral visualizations at the maximum instrumentation specificity, can easily be parallelized, and may use alternative metrics to emphasize different criteria.

Experiments

Data

MALDI MSI data was provided by Proteopath GmbH (Trier, Germany), who scanned Formalin Fixed Paraffin Embedded (FFPE) tissues, collected at the Medical Service Center for Histology, Cytology and Molecular Diagnostics (Trier, Germany) [2]. Imaging had used a Bruker rapifleX Tissuetyper (Bremen, Germany) in a positive-ion reflector mode, at a 100 µm spatial resolution, with $\bar{Z}_{low} = 600$, $\bar{Z}_{high} = 3200$, and where chemical noise analysis for mass alignment indicated a $\Delta = 20$ ppm. Given 7 ovary sample data, 5 were randomly chosen for training, the remaining 2 reserved for validation. Testing used 5 breast sample data, with the tissue type variation intended to emphasize model generalization capability. 10 *m/z*, denoting peptides of research interest, were identified through expert analysis, with an alternative set of 10 found through the FFS method. Fig. 2 shows visualizations of the *m/z* for a training sample. Visual inspection illustrates the FFS process succeeds in capturing similar molecular structures present in the expert choices.

Quantitative Evaluation

SLADS-LS, DLADS, and multimodal DLADS models were trained using expert-chosen *m/z*, with the latter having a second variant developed with the FFS set. MALDI MSI acquisitions of the testing samples, were then simulated, measuring up to ~30% FoV, in two scenarios: targeting 1) expert and 2) FFS *m/z* channel sets. Reconstructed visualizations, generated at 1% FoV intervals, of all measured ($\hat{X}_{\bar{Z}}$) and targeted ($\hat{X}_Z$) *m/z* were compared against the ground-truth ($X_{\bar{Z}}$ and X_Z), using PSNR. Results (Table 1) were averaged across all testing samples (Fig. 3), as an evaluation of final reconstruction quality, and integrated across the measured % FoV to obtain AUC scores, indicating overall sampling performance. Model effectiveness at forming ERD for targeted *m/z* ($\hat{R}_Z$) was similarly evaluated against RD (R_Z) (computed post-sampling) and summarized with PSNR-based AUC scores.

Sampling up to ~30% FoV with DLADS, targeted *m/z* reconstructions reached an average 30+ dB PSNR, matching with prior nano-DESI MSI results [11]. If the achieved quality were sufficient for a given research application, this would correspond to a 70% throughput improvement. Compared to SLADS-LS, DLADS better determined ERD by ~4%, which for both targeted and all *m/z* improved final reconstruction and AUC scores by ~1-2%.

Multimodal DLADS immediately reduced the average measurable area in the test samples by ~41% and at ~30% FoV yielded average ~5% and ~12% advancements on PSNR and AUC scores for targeted *m/z*. This indicates a benefit to the incorporation of structural information present in other modalities, as may possibly be obtained with confocal optical microscopes.

While targeting expert-selected *m/z*, with a multimodal DLADS model trained with FFS-based *m/z* and vice versa, both show negligible 0.1% differences to the AUC scores. Compared to expert-based *m/z* selections, the FFS process did not degrade performance, while being a more scalable and consistent option.

Table 1: Quantitative PSNR (dB) results for simulated acquisition averaged across all samples in the testing set

Testing $\bar{Z}$	Model	Training $\bar{Z}$	Multimodal	$\hat{R}_{\bar{Z}}$ AUC	$\hat{X}_{\bar{Z}}$ ~30% FoV	$\hat{X}_{\bar{Z}}$ AUC	$\hat{X}_Z$ ~30% FoV	$\hat{X}_Z$ AUC
Expert	SLADS-LS	Expert	False	712.50	36.89	928.14	31.97	793.17
	DLADS			740.41	37.57	933.79	32.57	804.98
			True	746.99	39.53	994.11	34.08	900.66
		FFS		750.26	39.29	993.74	33.91	900.41
FFS	SLADS-LS	Expert	False	803.38	37.93	935.67	32.11	780.96
	DLADS			828.46	38.63	941.80	32.63	793.07
			True	832.29	41.04	1023.91	34.22	901.03
		FFS		835.22	40.76	1022.52	34.06	900.27

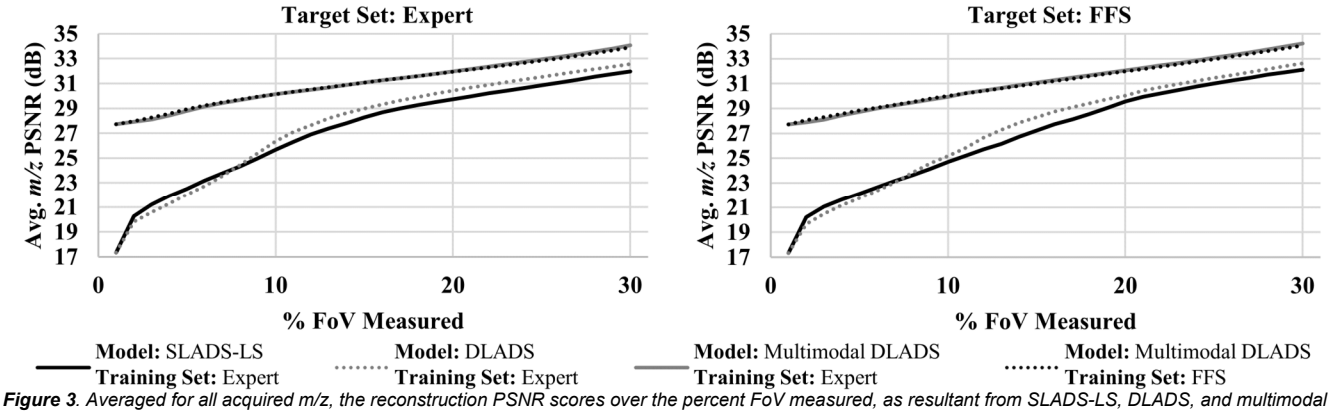

***Figure 3**. Averaged for all acquired m/z, the reconstruction PSNR scores over the percent FoV measured, as resultant from SLADS-LS, DLADS, and multimodal DLADS dynamic sparse sampling, either targeting expert-based m/z, or those found with the FFS process.*

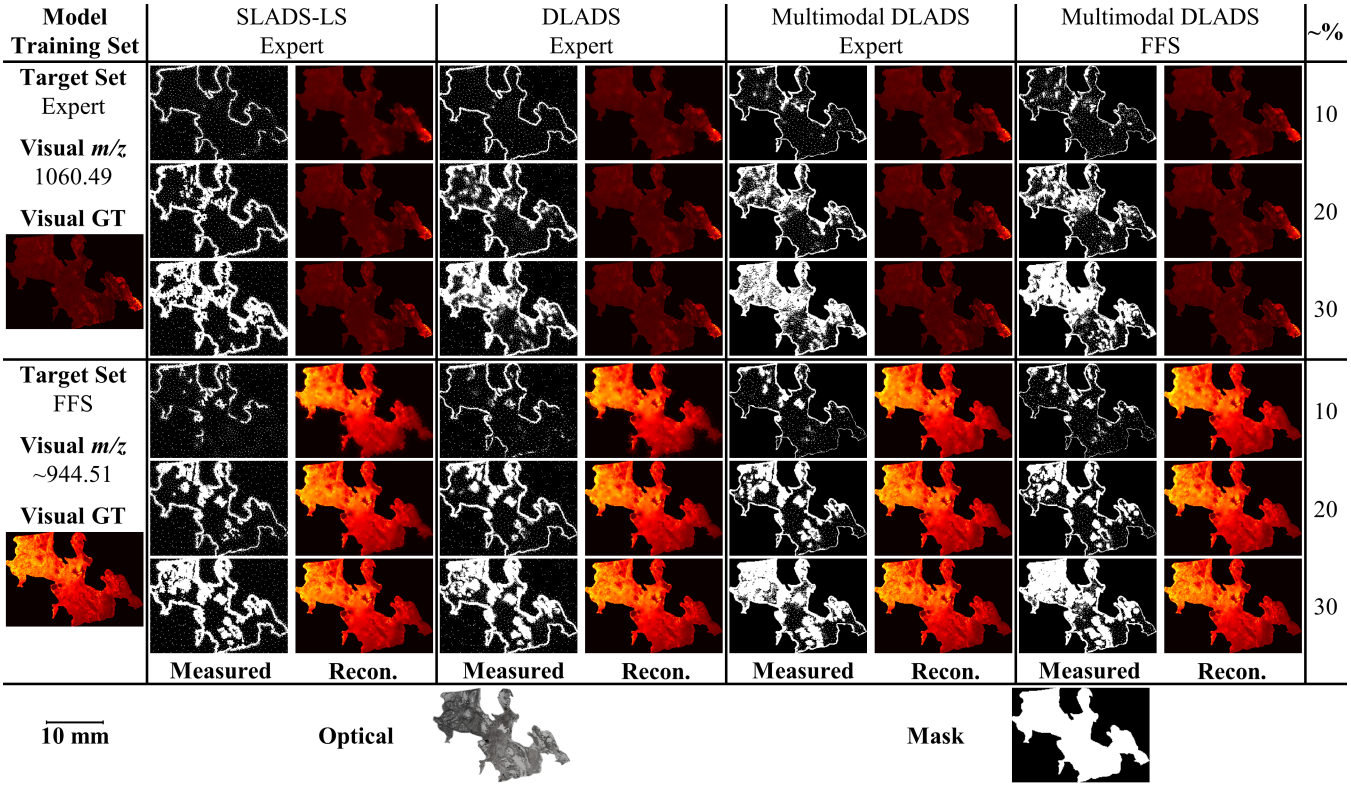

***Figure 4**. Ground-Truth (GT) visualizations from expert and FFS m/z sets, with corresponding m/z reconstructions (Recon.) and measurement masks (Measured) generated during simulated acquisition of a testing sample using SLADS-LS, DLADS, and multimodal DLADS.*

Qualitative Evaluation

Measurement masks and reconstructions of a test sample for example target *m/z* (Expert: 1060.49; FFS: ~944.51), at 10%, 20%, and 30% measured FoV are shown in Fig. 4. SLADS-LS demonstrates a greater tendency to oversample tissue edges, where DLADS manages to reduce this behavior. The incorporation of spatial relationships through convolutional layers, intrinsic to the DLADS U-Net architecture, yields more diverse location selection, with greater focus on localized structures. Multimodal DLADS further spreads measurement selections inside the tissue area. Even without using the optical image data, the algorithm quickly distinguishes and focuses on foreground regions, resulting in improved reconstruction quality. This points to a distinct benefit in integration of DLADS with MALDI MSI.

Regardless of training DLADS with expert or FFS *m/z* sets, the resultant sampling patterns are comparable. It may be noted that when any of the models targeted the FFS *m/z* set, there was a greater propensity to scan localized biological structures. This indicates that the FFS *m/z* set was less biased to particular tissue features. This behavior was not distinguishable through the utilized PSNR metrics since they quantify global image differences. It would be more beneficial, from a biological research perspective (e.g., proteomics), to emphasize the reconstruction quality of local structures.

Conclusions

This work simulated integration of multichannel and multimodal DLADS with MALDI MSI, achieving 30+ dB PSNR for reconstructions of targeted *m/z*, for ~70% throughput gains. A SSIM-based FFS *m/z* selection method was introduced as an alternative to expert annotation, achieving near-identical performance in testing. Integration of more modalities, such as optical imaging shows potential for additional performance gains.

While the DLADS CNN architecture demonstrated an advantage over SLADS-LS in regression, with positive effects to sampling patterns, this did not translate well in the final reconstruction PSNR scores. For future work, PSNR may need to be replaced with an alternative perceptual difference metric that can better quantify the relative quality of local structure reconstructions.

The FFS process may also be improved. Since the variance in cumulative SSIM scores decreases with each *m/z* channel selection, a cutoff value could be specified to determine how many *m/z* are actually needed to represent the underlying spectra. DLADS may also be able to use the determined SSIM scores to weight target *m/z* during acquisition, by their relative importance.

Lastly, DLADS remains bottlenecked by its approximation of RD for generation of static training datasets and continued reliance on IDW mean interpolation for reconstruction. There exists potential for overcoming these limitations through incorporation of novel network architectures, such as Generative Adversarial Networks (GANs), which should be pursued in future research.

Code

The DLADS and SLADS-LS programs, utilized in this study, have been made available at: github.com/Yatagarasu50469/SLADS, under GNU General Public License v3.0, as release v0.9.5.

Acknowledgement

The authors extend a special thanks to Jörg Kriegsmann and Rita Casadonte (Proteopath GmbH, Trier, Germany) for their roles in scanning, processing, sharing, and granting permission for using the tissue sample data herein relied upon.

References

[1] R. M. Caprioli, T. B. Farmer, and J. Gile, "Molecular Imaging of Biological Samples: Localization of Peptides and Proteins Using MALDI-TOF MS," *Analytical Chemistry*, vol. 69, no. 23, pp. 4751–4760, Dec. 1997, doi: https://doi.org/10.1021/ac970888i.

[2] T. Boskamp *et al.*, "Using the Chemical Noise Background in MALDI Mass Spectrometry Imaging for Mass Alignment and Calibration," vol. 92, no. 1, pp. 1301–1308, Dec. 2019, doi: doi.org/10.1021/acs.analchem.9b04473.

[3] G. M. D. Godaliyadda, D. H. Ye, M. D. Uchic, M. A. Groeber, G. T. Buzzard, and C. A. Bouman, "A Supervised Learning Approach for Dynamic Sampling," *Electronic Imaging*, vol. 28, no. 19, pp. 1–8, Feb. 2016, doi: doi.org/10.2352/issn.2470-1173.2016.19.coimg-153.

[4] G. M. D. P. Godaliyadda, "A Supervised Learning Approach for Dynamic Sampling (SLADS)," Ph.D. dissertation, Purdue University, 2017. [Online]. Available: docs.lib.purdue.edu/open_access_dissertations/1550

[5] N. M. Scarborough *et al.*, "Dynamic X-ray diffraction sampling for protein crystal positioning," vol. 24, no. 1, pp. 188–195, Jan. 2017, doi: doi.org/10.1107/s160057751601612x.

[6] S. Zhang *et al.*, "Dynamic Sparse Sampling for Confocal Raman Microscopy," vol. 90, no. 7, pp. 4461–4469, Mar. 2018, doi: doi.org/10.1021/acs.analchem.7b04749.

[7] G. M. Dilshan P. Godaliyadda, D. H. Ye, M. D. Uchic, M. A. Groeber, G. T. Buzzard, and C. A. Bouman, "A Framework for Dynamic Image Sampling Based on Supervised Learning," vol. 4, no. 1, pp. 1–16, Mar. 2018, doi: doi.org/10.1109/tci.2017.2777482.

[8] Y. Zhang, G. M. Dilshan P. Godaliyadda, N. J. Ferrier, Emine Begum Gulsoy, C. A. Bouman, and C. Phatak, "Reduced electron exposure for energy-dispersive spectroscopy using dynamic sampling," vol. 184, pp. 90–97, Jan. 2018, doi: doi.org/10.1016/j.ultramic.2017.10.015.

[9] D. Helminiak, H. Hu, J. Laskin, and D. H. Ye, "Deep Learning Approach for Dynamic Sparse Sampling for High-Throughput Mass Spectrometry Imaging," *Electronic Imaging*, 2021, doi: doi.org/10.2352/issn.2470-1173.2021.15.coimg-290.

[10] D. S. Helminiak, "Deep Learning Approach for Dynamic Sampling for High-Throughput Nano-DESI MSI," Master's Thesis, Marquette University, 2021. [Online]. Available: epublications.marquette.edu/theses_open/710/

[11] D. Helminiak, H. Hu, J. Laskin, and D. H. Ye, "Deep Learning Approach for Dynamic Sampling for Multichannel Mass Spectrometry Imaging," vol. 9, pp. 250–259, Jan. 2023, doi: doi.org/10.1109/tci.2023.3248947.

[12] H. Hu *et al.*, "High-Throughput Mass Spectrometry Imaging with Dynamic Sparse Sampling," vol. 2, no. 5, pp. 466–474, Aug. 2022, doi: doi.org/10.1021/acsmeasuresciau.2c00031.

[13] H. Hu, R. Yin, H. M. Brown, and J. Laskin, "Spatial Segmentation of Mass Spectrometry Imaging Data by Combining Multivariate Clustering and Univariate Thresholding," *Analytical Chemistry*, vol. 93, no. 7, pp. 3477–3485, Feb. 2021, doi: doi.org/10.1021/acs.analchem.0c04798.

[14] Z. Wang, A. C. Bovik, H. R. Sheikh, and E. P. Simoncelli, "Image Quality Assessment: From Error Visibility to Structural Similarity," *IEEE Transactions on Image Processing*, vol. 13, no. 4, pp. 600–612, Apr. 2004, doi: doi.org/10.1109/tip.2003.819861.

[15] Y. Zhang, X. Huang, N. Ferrier, E. Gulsoy, and C. Phatak, "U-SLADS: Unsupervised Learning Approach for Dynamic Dendrite Sampling," 2018, doi: 10.48550/arXiv.1807.02233.

[16] A. Horé and D. Ziou, "Image Quality Metrics: PSNR vs. SSIM," *2010 20th International Conference on Pattern Recognition*, Istanbul, Turkey, 2010, pp. 2366-2369, doi: doi.org/10.1109/ICPR.2010.579.

[17] F. J. Ferri, P. Pudil, M. Hatef, and J. Kittler, "Comparative Study of Techniques for Large-Scale Feature Selection." *Pattern Recognition in Practice IV - Multiple Paradigms, Comparative Studies and Hybrid Systems*, vol. 16, 1994, pp. 403–413, doi: doi.org/10.1016/b978-0-444-81892-8.50040-7.

[18] Z. Wang, A. C. Bovik, H. R. Sheikh, and E. P. Simoncelli, "Image Quality Assessment: From Error Visibility to Structural Similarity," *IEEE Transactions on Image Processing*, vol. 13, no. 4, pp. 600–612, Apr. 2004, doi: doi.org/10.1109/tip.2003.819861.

[19] O. Ronneberger, P. Fischer, and T. Brox, "U-Net: Convolutional Networks for Biomedical Image Segmentation," *Lecture Notes in Computer Science*, vol. 9351, pp. 234–241, 2015, doi: https://doi.org/10.1007/978-3-319-24574-4_28.

[20] D. Shepard, "A two-dimensional interpolation function for irregularly-spaced data," *Proceedings of the 1968 23rd ACM national conference*, 1968, doi: doi.org/10.1145/800186.810616.

Author Biography

David Helminiak is a Ph.D. candidate in the Electrical and Computer Engineering department at Marquette University, where he received an M.S. (2021) and two B.S. (2018) degrees. His research focuses on developing neural network architectures for interdisciplinary applications of artificial intelligence and machine learning.

Tobias Boskamp is the head of SCiLS R&D at Bruker Corporation. He received his Dr. rer. nat. (2003) from the University of Bremen, Diplom (1994) from the Technical University of Berlin, and Vordiplom (1988) at the University of Düsseldorf. His research incorporates medical image processing and analysis.

Dong Hye Ye is an Assistant Professor in the Department of Computer Science at Georgia State University. He received his Ph.D. (2013) from the University of Pennsylvania, M.S. (2008) from the Georgia Institute of Technology, and B.S. (2007) at Seoul National University. His research includes sparse sampling for microscopic imaging, iterative tomographic reconstruction, and UAV sensing via machine learning.